

Orange-Emitting $\text{Li}_4\text{Sr}_4[\text{Si}_4\text{O}_4\text{N}_6]\text{O}:\text{Eu}^{2+}$ —a Layered Lithium Oxonitridosilicate Oxide

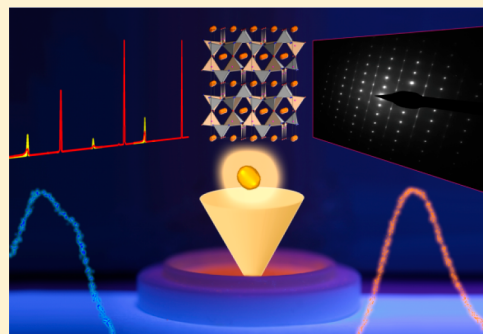
Robin Niklaus,[†] Lukas Neudert,[†] Juliane Stahl,[†] Peter J. Schmidt,[‡] and Wolfgang Schnick^{*,†}

[†]Department of Chemistry, University of Munich (LMU), Butenandtstrasse 5–13, 81377 Munich, Germany

[‡]Lumileds Germany GmbH, Lumileds Phosphor Center Aachen, Philipsstrasse 8, 52068 Aachen, Germany

Supporting Information

ABSTRACT: We report on the structure and properties of the lithium oxonitridosilicate oxide $\text{Li}_4\text{Sr}_4[\text{Si}_4\text{O}_4\text{N}_6]\text{O}:\text{Eu}^{2+}$ obtained from solid-state metathesis. The crystal structure was solved and refined from single-crystal X-ray data in the space group $P4_2/nmc$ (No. 137) [$Z = 2$, $a = 7.4833(6)$, $c = 9.8365(9)$ Å, and $R1(\text{obs}) = 0.0477$]. The structure of $\text{Li}_4\text{Sr}_4[\text{Si}_4\text{O}_4\text{N}_6]\text{O}:\text{Eu}^{2+}$ is built up from a layered 2D network of SiN_3O tetrahedra and exhibits stacking disorder. The results are supported by transmission electron microscopy and energy-dispersive X-ray spectroscopy as well as lattice energy, charge distribution, and density functional theory (DFT) calculations. Optical measurements suggest an indirect band gap of about 3.6 eV, while DFT calculations on a model free of stacking faults yield a theoretical electronic band gap of 4.4 eV. Samples doped with Eu^{2+} exhibit luminescence in the orange spectral range ($\lambda_{\text{em}} \approx 625$ nm; full width at half-maximum ≈ 4164 cm^{-1} ; internal quantum efficiency at room temperature = 24%), extending the broad field of phosphor materials research toward the sparsely investigated materials class of lithium oxonitridosilicate oxides.



INTRODUCTION

The increase of the complexity with regard to the elemental and structural compositions of nitride phosphor materials has recently led to unexpected multinary phosphors like $\text{Li}_{38.7}\text{RE}_{3.3}\text{Ca}_{5.7}[\text{Li}_2\text{Si}_{30}\text{N}_{59}]\text{O}_2\text{F}:\text{Ce}^{3+}$ (RE = La, Ce, Y).¹ This process forebodes the importance of extending fundamental research toward similar complex systems by offering a number of tunable set screws in terms of composition and structural phenomena, which, in turn, can influence the materials properties. However, because of the difficulty of targeted synthesis toward phosphor materials from scratch, it ever so often resembles a roll of the dice. This is partly because of a number of competing reactions and possible thermodynamic sinks. This makes it difficult to control the synthesis and respective formation conditions of such multinary component systems, which often leads to microcrystalline samples. However, high-throughput screening methods like single-particle diagnosis in combination with transmission electron microscopy (TEM) can help to facilitate the identification of novel compounds for which structure determination is not straightforward, such as $\text{La}_{24}\text{Sr}_{14-7x}[\text{Si}_{36}\text{N}_{72}](\text{O}_{1-x}\text{F}_x)_{14}$ ($x = 0.489$).^{2,3} The subsequent migration into conventional synthetic optimization strategies, upon the identification of promising materials, can then be used to optimize bulk synthesis. With regard to maintaining at least a partially directed synthesis approach, phosphor host structures such as $\text{Li}_2\text{Ca}_2[\text{Mg}_2\text{Si}_2\text{N}_6]$, $\text{Ca}_3\text{Mg}[\text{Li}_2\text{Si}_2\text{N}_6]$, and $\text{Ca}_2\text{Mg}[\text{Li}_4\text{Si}_2\text{N}_6]$ exemplify that formal substitution of alkaline-earth metals by significantly smaller and lighter cations such as Li appears

promising in order to increase the structural diversity, while maintaining fundamental structure motifs.^{4–6} That is, these compounds can all be considered to be Ca-substituted variants of $\text{Ca}_5[\text{Si}_2\text{N}_6]$. Similar analogies are known from Li-substituted garnet-type materials, which have led to a number of suitable solid electrolytes.^{7–9} This coincides with a general trend to incorporate Li into phosphor host structures because it may function both as a counteranion like in $\text{Li}_2\text{Ca}_2[\text{Mg}_2\text{Si}_2\text{N}_6]$ and $\text{Ca}_{18.75}\text{Li}_{10.5}[\text{Al}_{39}\text{N}_{55}]$ and as part of the anionic network like in $\text{Sr}[\text{LiAl}_3\text{N}_4]$, $\text{Sr}_4[\text{LiAl}_{11}\text{N}_{14}]$, or $\text{Ca}_3\text{Mg}[\text{Li}_2\text{Si}_2\text{N}_6]$.^{4,5,10–13} All of which exhibit interesting luminescence properties upon Eu^{2+} or Ce^{3+} doping with auxiliary examples such as $\text{LiSi}_2\text{N}_3:\text{Eu}^{2+}$, $\text{Ba}[\text{Li}_2(\text{Al}_2\text{Si}_2)\text{N}_6]:\text{Eu}^{2+}$, and $\text{Ba}_2\text{LiSi}_7\text{AlN}_{12}:\text{Eu}^{2+}$ at hand.^{14–16} Undeniably, Li-containing nitridosilicates have attracted a lot of attention in recent years as novel phosphor materials.

With regard to the exploration of new and diverse anionic networks and frameworks, the extensive study of oxonitridosilicates has further promoted the synthesis of Eu-doped phosphor materials such as β -sialon, and the layered materials $(\text{Sr},\text{Ba})\text{Si}_2\text{O}_2\text{N}_2$ and $\text{RE}_{26}\text{Ba}_6[\text{Si}_{22}\text{O}_{19}\text{N}_{36}]\text{O}_{16}$ (RE = Y, Tb).^{17–22} $\text{M}(\text{Si}_2\text{O}_2\text{N}_2)$ (M = Ca, Sr, Ba) represents an excellent example as to how the choice of the cation may further impact the structural properties. Alterations of layers and metal coordination are introduced upon going from $\text{CaSi}_2\text{O}_2\text{N}_2$ ($P2_1$) to $\text{SrSi}_2\text{O}_2\text{N}_2$ ($P1$) and $\text{BaSi}_2\text{O}_2\text{N}_2$ ($Pbcn$), impacting the luminescence properties upon Eu^{2+} doping.

Received: August 23, 2018

Concurrently, additional intergrowth occurs upon different mixed occupation ratios on the (Sr, Ba) site between the latter two.^{21,23} Especially for such layered compounds, real structure phenomena such as stacking disorder and intergrowth can pose major obstructions upon structure determination in the absence of suitable single crystals or even in the attempted confirmation of bulk syntheses. Challenges can be successfully tackled by advanced analytical methods such as aberration-corrected TEM. Next to a detailed elucidation of the latter compounds by various TEM methods, applications comprise the elucidation of modulated structures and the differentiation of heavy cations with a roentgenographically similar Z-contrast.^{3,20,24} In this contribution, we present the synthesis and characterization of the novel orange luminescent layered lithium oxonitridosilicate oxide $\text{Li}_4\text{Sr}_4[\text{Si}_4\text{O}_4\text{N}_6]\text{O}:\text{Eu}^{2+}$, extending the sparse field of lithium oxonitridosilicate compounds. The structure was solved by single-crystal X-ray diffraction (XRD). TEM investigations confirm the elemental composition and cell metrics while revealing low-level stacking disorder in the *ab* plane in both single crystals and bulk samples.

Electronic and mechanical properties were calculated by subsidiary density functional theory (DFT) calculations. Our study combines different interlocking analytical methods that together allow for concluding discussions on the possible impact of real-structure phenomena on the resulting luminescence properties relevant to future materials design considerations.

EXPERIMENTAL SECTION

Synthesis. All synthesis steps were performed in an argon-filled glovebox (Unilab, MBraun, Garching; $\text{O}_2 < 1$ ppm; $\text{H}_2\text{O} < 1$ ppm) or in flame-dried glassware on a Schlenk line. The screening of different product mixtures yielded a minority phase of single crystals of $\text{Li}_4\text{Sr}_{3.62}\text{Eu}_{0.38}[\text{Si}_4\text{O}_4\text{N}_6]\text{O}$ from reacting a composite mixture of SrF_2 (0.17 mmol, 21.7 mg, Sigma-Aldrich, 99.99%), “ $\text{Si}(\text{NH})_2$ ” (0.18 mmol, 10.6 mg), LiN_3 (0.38 mmol, 19 mg), Mn (0.84 mmol, 46.4 mg, Alfa Aesar, 99.95%), and EuF_3 (0.009 mmol, 1.8 mg, Sigma-Aldrich, 99.99%).^{25,26} The ground starting materials were placed in a Ta ampule, which was supposedly contaminated with traces of O during welding. The ampule was placed in a tube furnace under vacuum, heated to 950 °C at 5 K min^{-1} , and kept at 950 °C for 32 h before the furnace was turned off. The yellow-to-orange single crystals were identified out of the heterogeneous product by UV illumination. Following structure determination, the synthesis was optimized to obtain bulk samples of $\text{Li}_4\text{Sr}_4[\text{Si}_4\text{O}_4\text{N}_6]\text{O}:\text{Eu}^{2+}$. Powder samples of $\text{Li}_4\text{Sr}_4[\text{Si}_4\text{O}_4\text{N}_6]\text{O}$ were synthesized from SrF_2 (0.18 mmol, 22.2 mg; Sigma-Aldrich, 99.99%), SrH_2 (0.18 mmol, 15.9 mg; Materion, 99.7%), LiN_3 (0.363 mmol, 17.8 mg), $\text{Li}(\text{NH}_2)$ (0.206 mmol, 7.6 mg, Sigma-Aldrich, 95%), Li_2O (0.45 mmol, 13.56 mg, Schuchardt, 98%), and “ $\text{Si}(\text{NH})_2$ ” (0.36 mmol, 21.1 mg). CsI (0.2 mmol, 53 mg, Chempur, 99.9%) was used as a flux. The starting materials were thoroughly ground in an agate mortar and filled into a Nb ampule. The ampule was subsequently welded shut and placed in a tube furnace (type AXIO 10/450, Hüttinger Elektronik, Freiburg, Germany; maximal electrical output 10 kW), heated under vacuum to 900 °C for 3 h, maintained at that temperature for 32 h, and finally quenched to room temperature by switching off the furnace. The resulting product was washed with dry ethanol to remove excess CsI. The filter residue yielded a colorless mixture of variable amounts of LiF, Li_2SiN_2 , and nanocrystalline $\text{Li}_4\text{Sr}_4[\text{Si}_4\text{O}_4\text{N}_6]\text{O}$ as the majority phase. The addition of EuF_3 during synthesis with a nominal concentration of 1 mol % Eu related to Sr yielded a powder of $\text{Li}_4\text{Sr}_4[\text{Si}_4\text{O}_4\text{N}_6]\text{O}:\text{Eu}^{2+}$ with yellow body color. All such samples show strong yellow-orange luminescence under irradiation with blue

light. Doped and nondoped products are stable toward O_2 yet sensitive to the extended exposure of water.

Single-Crystal XRD. Single crystals of $\text{Li}_4\text{Sr}_4[\text{Si}_4\text{O}_4\text{N}_6]\text{O}:\text{Eu}^{2+}$ were isolated and mounted on MicroMounts (MiTeGen) with an aperture size of 20 μm . XRD data were measured with a Bruker D8 Venture diffractometer with a rotating anode (Mo $K\alpha$ radiation). Absorption correction was performed using SADABS.²⁷ The crystal structure was solved using direct methods (SHELXS) and refined by a least-squares method (SHELXL).^{28–30} Details on the crystal structure investigation can be obtained from the Cambridge Crystallographic Data Centre (CCDC) upon quoting the CCDC code 1862968.

Powder XRD (PXRD). PXRD measurements were carried out on ground samples, which were loaded into silica glass capillaries of 0.2 mm diameter with a wall thickness of 0.01 mm (Hilgenberg GmbH, Malsfeld, Germany). Diffraction data were obtained using a STOE STADI P diffractometer [Cu $K\alpha_1$ radiation, Ge(111) monochromator, Mythen1K detector] in modified parafocusing Debye–Scherrer geometry. Rietveld refinements were carried out with TOPAS Academic V4.1 software by applying the fundamental parameters approach (direct convolution of source emission profiles, axial instrument contributions, crystallite size, and microstrain effects).^{31–34} Preferred orientation was taken into account by using fourth-order spherical harmonics, and anisotropic broadening of the reflection profiles was refined using the LeBail–Jouanneaux algorithm.³⁵ Absorption effects were corrected using the calculated absorption coefficient from XRD refinements.

UV/Vis Spectroscopy. A diffuse-reflectance spectrum of $\text{Li}_4\text{Sr}_4[\text{Si}_4\text{O}_4\text{N}_6]\text{O}$ was measured with a Jasco V-650 UV/vis spectrophotometer in the range of 240–800 nm with a 5 nm step size. The device is equipped with a deuterium/halogen lamp (Czerny–Turner monochromator with 1200 lines mm^{-1} concave grating, photomultiplier tube detector).

Fourier Transform Infrared (FTIR) Spectroscopy. FTIR spectroscopy on $\text{Li}_4\text{Sr}_4[\text{Si}_4\text{O}_4\text{N}_6]\text{O}:\text{Eu}^{2+}$ was carried out with a Perkin Elmer BXII spectrometer using the attenuated-total-reflectance (ATR) method.

Computational Details. The structural relaxation of $\text{Li}_4\text{Sr}_4[\text{Si}_4\text{O}_4\text{N}_6]\text{O}$ was performed with the Vienna ab initio simulation package (VASP).^{36–38} The total energy of the unit cell was converged to 10^{-7} eV/atom with residual atomic forces below 5×10^{-3} eV Å^{-1} . The exchange correlation was treated within the generalized gradient approximation (GGA) of Perdew, Burke, and Ernzerhof and the projector-augmented-wave method.^{39–42} A plane-wave cutoff of 535 eV was chosen for calculations with a Brillouin zone sampling on a Γ -centered *k*-mesh produced from the method of Monkhorst and Pack of $7 \times 7 \times 6$.⁴³ Additional calculations were performed with the modified Becke–Johnson formalism (GGA-*mbj*) to treat the electronic band gap.^{44–46} In order to obtain elastic constants and moduli, calculations of the elastic tensors were conducted by deriving the stress–strain relationship from six finite lattice distortions of the crystal utilizing displacements of ± 0.015 Å .⁴⁷

Luminescence. Photoluminescence measurements were performed on nanocrystalline powder samples in poly-(tetrafluoroethylene) sample holders using an in-house-built system based on a 5.3-in. integrating sphere and a spectrofluorimeter equipped with a 150 W Xe lamp and two 500 mm Czerny–Turner monochromators (1800 grooves mm^{-1} and 250/500 nm blaze gratings) with a spectral range from 230 to 820 nm. The internal quantum efficiency (IQE) of the samples was determined by comparing integrated emission intensities and absorption at excitation wavelength with standard materials (BaSO_4 , Merck, for white standard DIN 5033; commercial $(\text{Sr,Ca})\text{AlSiN}_3:\text{Eu}^{2+}$, Mitsubishi Chemical, and $\text{Y}_3\text{Al}_5\text{O}_{12}:\text{Ce}^{3+}$, Philips) at room temperature. Thermal quenching of the emission was investigated with an AvaSpec-2048 spectrometer and a stabilized light-emitting-diode (LED) light source (450 nm) for sample excitation. Samples were measured in a temperature range from room temperature to 330 °C with a step size of ≈ 24 °C in Cu-plated sample holders that were temperature-controlled with an IR lamp. The cryospectroscopy setup covers the range from 300 to 6 K. The measurement was performed on a thick-

bed powder layer of the specimen positioned in an evacuated cooling chamber. Cooling was done via a liquid-He compressor system from Advance Research System Inc. (ARS4HW). The samples were measured by a fiber-coupled spectroscopy system containing a thermally stabilized LED light source and a fiber-optic spectrometer from Ocean Optics (HR2000+ES).

TEM. The TEM investigations were done on crystallites originating from several samples of $\text{Li}_4\text{Sr}_4[\text{Si}_4\text{O}_4\text{N}_6]\text{O}:\text{Eu}^{2+}$. The crystals were crushed and suspended in ethanol and then drop-casted onto a Cu grid covered with a holey C film (PLANO GmbH, Wetzlar, Germany). TEM experiments were performed on a Titan Themis 60-300 microscope (FEI, Hillsboro, OR) operated at a 300 kV acceleration voltage and equipped with an X-FEG, monochromator, C_s corrector, and windowless four-quadrant Super-X EDX detector (acquisition time 45 s). The TEM images were recorded using a $4\text{K} \times 4\text{K}$ Ceta CMOS camera (FEI, Hillsboro, OR). For data evaluation, the following software were used: *Digital Micrograph* and *ProcessDiffraction7* [geometric calculations for selected-area electron diffraction (SAED)], *JEMS* (SAED simulations), and *ES Vision* (evaluation of the EDX spectra).^{48–51}

RESULTS AND DISCUSSION

Synthesis and Chemical Analysis. For the synthesis of $\text{Li}_4\text{Sr}_4[\text{Si}_4\text{O}_4\text{N}_6]\text{O}:\text{Eu}^{2+}$, highly reactive starting materials such as SrF_2 , “ $\text{Si}(\text{NH})_2$ ”, SrH_2 , and EuF_3 were used. The synthesis route yields typically nanocrystalline aggregates with single-crystal sizes of approximately $1\ \mu\text{m}$ on average. A few crystals of larger size ($\approx 10\ \mu\text{m}$) could be isolated for single-crystal analysis from a single reaction batch. The composition could be corroborated by TEM–EDX measurements on representative crystals of different batches (Table S1). ATR-IR spectroscopy further indicates the absence of N–H groups (Figure S1).

Crystal Structure. The crystal structure of $\text{Li}_4\text{Sr}_4[\text{Si}_4\text{O}_4\text{N}_6]\text{O}:\text{Eu}^{2+}$ was solved and refined in the space group $P4_2/nmc$ (No. 137). All atoms aside from Li were refined anisotropically. The crystallographic details are given in Table 1.

Additional crystallographic information is given in Tables S2–S4. The crystal structure within the unit cell and different

structure motifs of $\text{Li}_4\text{Sr}_4[\text{Si}_4\text{O}_4\text{N}_6]\text{O}:\text{Eu}^{2+}$ are depicted in Figure 1a–d. The structure is composed of a layerlike network of doubly bridging Q^3 -type SiN_3O tetrahedra stacked along [001].

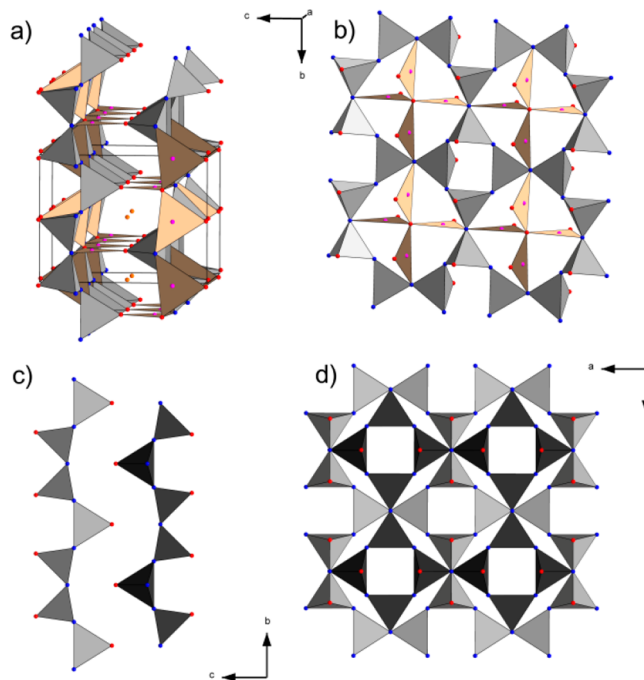


Figure 1. Different projections of the crystal structure of $\text{Li}_4\text{Sr}_4[\text{Si}_4\text{O}_4\text{N}_6]\text{O}:\text{Eu}^{2+}$ with SiN_3O tetrahedra (gray/black), N atoms (blue), O atoms (red), Li atoms (pink), and mixed Sr/Eu atoms (orange). (a) Projection along nearly [001] with the unit cell outlined in black. (b) Representation of a single layer forming *vierer* and *achter* rings enclosing trigonal-planar-coordinated Li. (c and d) Representation of SiN_3O layers along [100] (c) and [001] (d) illustrating the layered composition.

The atomic ratio $\text{Si}:(\text{O}/\text{N})$ within the network is 2:5, which corresponds to the regular value found in single-layer silicates.⁵² The crystal structure of $\text{Li}_4\text{Sr}_4[\text{Si}_4\text{O}_4\text{N}_6]\text{O}:\text{Eu}^{2+}$ exhibits motifs very similar to those of the previously reported nitridosilicate nitride $\text{Li}_2\text{Sr}_4[\text{Si}_2\text{N}_5]\text{N}$ (space group $I4\bar{m}2$).⁵³ Its structural relationship can be formally understood by the removal of half of the Sr atoms in the layered interspace of $\text{Li}_2\text{Sr}_4[\text{Si}_2\text{N}_5]\text{N}$ combined with a 180° twist of every second layer. In $\text{Li}_4\text{Sr}_4[\text{Si}_4\text{O}_4\text{N}_6]\text{O}:\text{Eu}^{2+}$, an additional isolated O atom is located centric of each *achter* ring. The cation coordination polyhedra are depicted in Figure 2. The Sr/Eu site is coordinated in the interspace of the layered network by O and N atoms of the SiN_3O tetrahedra, forming a distorted Johnson polyhedron (J_{49}). Li is coordinated trigonal-planar by the isolated O atom, and the N and terminal O atoms of two independent SiN_3O tetrahedra. The prolate nature of the O displacement ellipsoid of the isolated O2 is likely to originate from its higher degree of vibrational freedom compared to anions of the rigid and covalent oxonitridosilicate network. A possible split position and partial occupancy were further ruled out from difference Fourier mapping (Figure S2). CHARDI analysis further corroborates the cation assignment (Table S5).

The values for the tetrahedral bond lengths range from $1.692(3)\ \text{\AA}$ (Si–O) to $1.708(2)$ – $1.712(8)\ \text{\AA}$ (Si–N), in good agreement with values found in comparable oxonitridosilicate

Table 1. Crystallographic Data of the Single-Crystal Structure Determination of $\text{Li}_4\text{Sr}_{3.62(3)}\text{Eu}_{0.38(3)}[\text{Si}_4\text{O}_4\text{N}_6]\text{O}$

| | |
|---|--|
| refined composition | $\text{Li}_4\text{Sr}_{3.62(3)}\text{Eu}_{0.38(3)}[\text{Si}_4\text{O}_4\text{N}_6]\text{O}$ |
| formula mass [g mol^{-1}] | 679(2) |
| cryst syst | tetragonal |
| space group | $P4_2/nmc$ (No. 137) |
| lattice param [\AA] | $a = 7.4833(6)$, $c = 9.8365(9)$ |
| cell volume [\AA^3] | 550.84(10) |
| formula units/unit cell | 2 |
| X-ray density [g cm^{-3}] | 4.096 |
| abs coeff [$\mu\ \text{mm}^{-1}$] | 20.033 |
| abs corr | multiscan |
| diffractometer | Bruker D8 Venture |
| Mo $K\alpha$ radiation [\AA] | $\lambda = 0.71073$ |
| $F(000)$ | 623 |
| θ range [deg] | $3.421 \leq \theta \leq 30.497$ |
| indep reflns | 475 [$R_{\text{int}} = 0.0430$] |
| refined parameters/restraints | 35/0 |
| GoF | 1.094 |
| R1 [all data/for $I > 2\sigma(I)$] | 0.0477/0.0282 |
| wR2 [all data/for $I > 2\sigma(I)$] | 0.0633/0.0576 |
| $\Delta\rho_{\text{max}}/\Delta\rho_{\text{min}}$ (e \AA^{-3}) | 0.59/−0.75 |

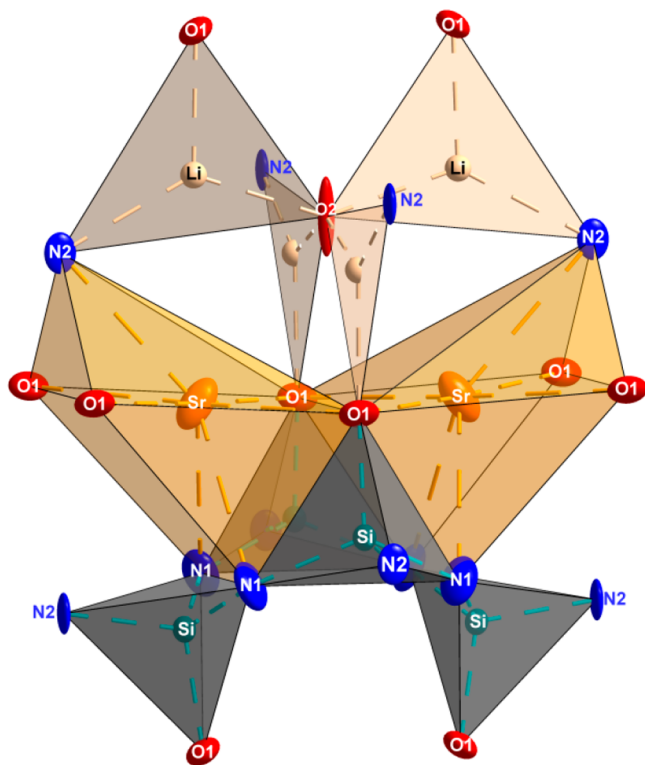


Figure 2. Coordination spheres of the Sr, Si, and Li atom sites in $\text{Li}_4\text{Sr}_4[\text{Si}_4\text{O}_4\text{N}_6]\text{O}:\text{Eu}^{2+}$. Displacement ellipsoids shown with 90% probability. Color code: Sr/Eu, orange; Si, turquoise; Li, ivory; O, red; N, blue.

compounds like $\text{Ce}_4[\text{Si}_4\text{O}_4\text{N}_6]\text{O}$ or $\text{SrSi}_2\text{O}_2\text{N}_2$.^{52,54} The same applies for the Sr–O [2.580(2)–2.717(2) Å], Sr–N [2.833(4)–2.846(2) Å], Li–O [1.955(8)–1.967(8) Å], and Li–N [2.142(8) Å] interatomic distances.^{53,55} In order to determine the composition of the samples, a Rietveld refinement has been carried out based on a PXRD pattern from an optimized synthesis bulk sample. A representative refinement is seen in Figure 3. It indicates $\text{Li}_4\text{Sr}_4[\text{Si}_4\text{O}_4\text{N}_6]\text{O}:\text{Eu}^{2+}$ as the majority phase ($\approx 84\%$) next to small amounts of side phases like Li_2SiN_2 and LiF. A few minor unknown reflections were observed that could not be assigned or indexed. Furthermore, a broadening and intensity misfit for the reflections (011), (012), and (211) was observed. Hence, in order to corroborate the chemical composition, single-crystal unit-cell parameters, ruling out unidentified superstructures and in order to reveal further possible real-structure phenomena, TEM investigations were conducted. Investigations comprise different bulk samples along with the single crystals used for X-ray structure determination.

TEM and EDX. From a representative SAED tilt series of crystallites, as depicted in Figure 4, it was possible to determine the unit-cell parameters (tetragonal with $a = 7.4$ Å and $c = 9.7$ Å). They agree with the unit-cell parameters from X-ray structure determination. In accordance with Laue class 4/ mmm , the SAED patterns along the zone axes [100], [110], and [011] show $mm2$ symmetry, and the reflection intensities approximately match those of the corresponding kinematical simulations (Figure 4, bottom). EDX measurements on several crystallites of $\text{Li}_4\text{Sr}_4[\text{Si}_4\text{O}_4\text{N}_6]\text{O}:\text{Eu}^{2+}$ further corroborate the chemical composition (Table S1).

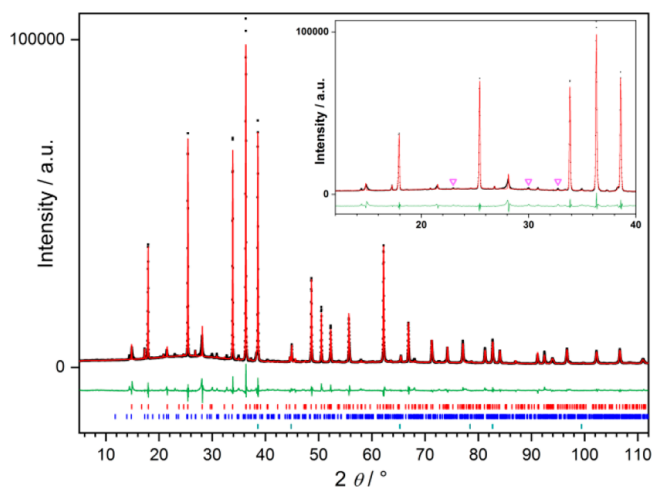


Figure 3. Rietveld refinement for a washed sample of $\text{Li}_4\text{Sr}_4(\text{Si}_4\text{O}_4\text{N}_6)\text{O}:\text{Eu}^{2+}$. Experimental data are in black, the Rietveld fit is the red line, and the difference plot is the green line. Minor unknown reflections (purple) are highlighted as triangles in the inset. Intensity misfits can be explained by stacking faults as observed by HRTEM investigations. Reflection positions for $\text{Li}_4\text{Sr}_4(\text{Si}_4\text{O}_4\text{N}_6)\text{O}:\text{Eu}^{2+}$ (red bars, 84 wt %), Li_2SiN_2 (blue bars, 5 wt %), and LiF (green bars, 11 wt %).

Additional diffuse intensity along $[001]^*$ was observed in zone axes perpendicular to c like [100], [110], and [120]. It is likely that the diffuse intensity is caused by structural differences in the ab planes stacked along c . Figure 5 depicts HRTEM investigations on thicker crystallites of the sample from which the single crystal was taken and where the diffuse intensity is more visible. It could be shown that areas of approximately 100 nm^2 are enough to cause diffuse intensity in the corresponding Fourier transforms similar to SAED (see its magnification in Figure S3). This is in agreement with the fact that no diffuse intensities could be observed for such crystallites with very thin crystal areas (Figure S4). The observation of diffuse scattering can be in line with the broadening of reflections in the PXRD patterns and corroborates an assumed stacking disorder. Subsequently, this effect could be approximated by DIFFaX simulations by the introduction of stacking faults of about 2.5% impacting the reflections in question, as shown in Figure 6.⁵⁶ The chosen stacking variant along with the matrix–vector relationship to the original layer is found in Figure S5.

MAPLE. The assignment of O and N from single-crystal refinement was further corroborated by calculations of the lattice energies by the MAPLE concept.^{57–60} Results are shown in Table 2. The total MAPLE value is in good agreement ($\Delta_E = 0.36\%$) with the one obtained by formation from binary compounds. Furthermore, partial MAPLE values of the different atoms are in the typical range of comparable compounds in the literature, confirming the chosen N, O, and Li assignments.^{53,61} For $\text{O}2^{[0]}$, there is no corresponding range of MAPLE values, but lowered values with respect to O atoms of higher bridging degree have been observed for other oxonitridosilicate oxides before.^{52,62,63} We therefore conclude that the lowered MAPLE value for O2 derives first from it not being incorporated into the rigid nitridosilicate network and second from its prolate displacement ellipsoid not being described accurately by point-charge approximations.

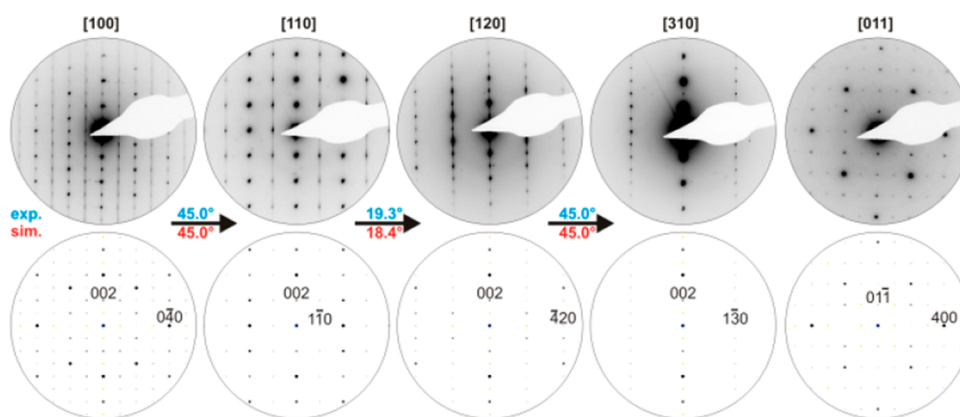


Figure 4. SAED tilt series of a representative crystallite of $\text{Li}_4\text{Sr}_4[\text{Si}_4\text{O}_4\text{N}_6]\text{O}:\text{Eu}^{2+}$ with experimental patterns (top) and tilt angles (blue) as well as simulated patterns (bottom) and tilt angles (red) based on the refined structure model from single-crystal X-ray data. Selected reflections are labeled with indices. Diffuse intensities are observed along $[001]$.

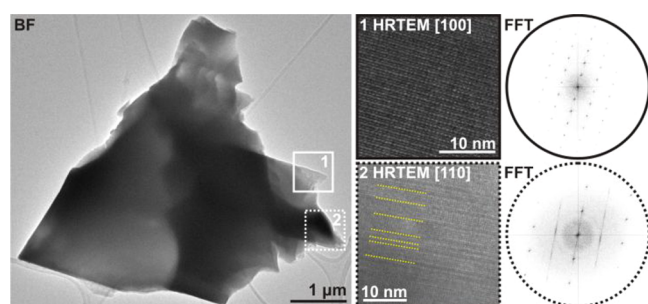


Figure 5. Bright-field image (left) and HRTEM images viewed along the $[100]$ and $[110]$ zone axes (middle) with corresponding Fourier transforms (right). Thin area 1 (highlighted by the solid line) shows no diffuse intensity in contrast to the thicker area 2 (highlighted by the dotted line). Contrast variations perpendicular to c possibly caused by defect layers are highlighted in yellow.

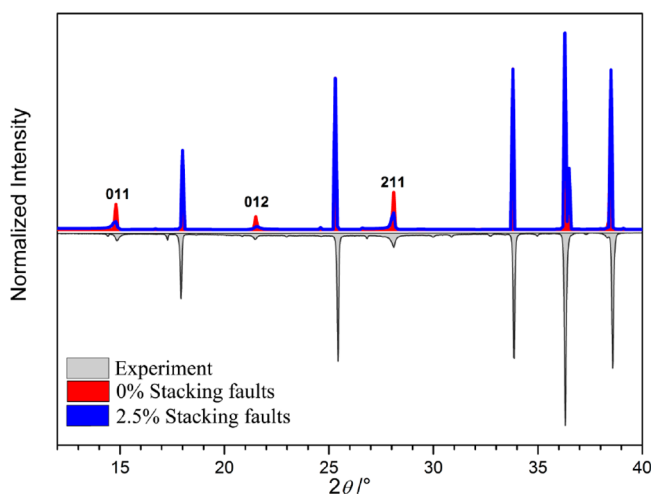


Figure 6. DIFFaX simulation of a possible stacking variant of $\text{Li}_4\text{Sr}_4[\text{Si}_4\text{O}_4\text{N}_6]\text{O}:\text{Eu}^{2+}$ indicating a broadening of selected reflections upon the introduction of low levels of stacking faults. Simulation based on a structure from single-crystal data.

DFT Calculations. In order to calculate the electronic band gap and mechanical properties of $\text{Li}_4\text{Sr}_4[\text{Si}_4\text{O}_4\text{N}_6]\text{O}$, we performed additional DFT calculations.

Electronic Structure. Calculations of the electronic density of states for $\text{Li}_4\text{Sr}_4[\text{Si}_4\text{O}_4\text{N}_6]\text{O}$ are depicted in Figure

Table 2. Results of the MAPLE Calculations (kJ mol^{-1}) for $\text{Li}_4\text{Sr}_4[\text{Si}_4\text{O}_4\text{N}_6]\text{O}^\alpha$

| | $\text{Li}_4\text{Sr}_4[\text{Si}_4\text{O}_4\text{N}_6]\text{O}$ |
|---|---|
| Sr^{2+} | 1666.653 |
| Si^{4+} | 9719.430 |
| Li^+ | 864.558 |
| $\text{N}1^{[2]}$ | 5464.986 |
| $\text{N}2^{[2]}$ | 5401.430 |
| $\text{O}1^{[1]}$ | 2469.910 |
| $\text{O}2^{[0]}$ | 1550.042 |
| total MAPLE | 93139 kJ mol^{-1} |
| $\frac{4}{3}\text{Si}_3\text{N}_4 + 4\text{SrO} + \text{Li}_2\text{O} + \frac{2}{3}\text{Li}_3\text{N}$ | 93479 kJ mol^{-1} |

^aTypical partial MAPLE values (kJ mol^{-1}): Sr^{2+} , 1500–2300; Si^{4+} , 9000–10200; $\text{N}^{[2]3-}$, 4600–6000; Li^+ , 550–860; $\text{O}^{[1]2-}$, 2000–2800.

7. $\text{Li}_4\text{Sr}_4[\text{Si}_4\text{O}_4\text{N}_6]\text{O}$ exhibits insulating properties with an electronic band gap of about 4.4 eV. This increase compared to

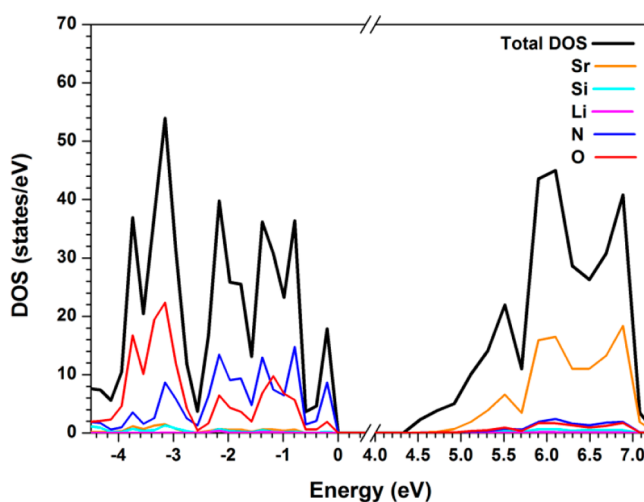


Figure 7. Density of states of $\text{Li}_4\text{Sr}_4(\text{Si}_4\text{O}_4\text{N}_6)\text{O}$ as calculated with the mBJ functional.

that of $\text{Li}_2\text{Sr}_4(\text{Si}_2\text{N}_5)\text{N}$, which was estimated to have an E_g of about 2.4 eV, can possibly be attributed to the removal of one Sr layer within $\text{Li}_4\text{Sr}_4[\text{Si}_4\text{O}_4\text{N}_6]\text{O}$. The elastic constants, resulting moduli, and Debye temperature (θ_D) are depicted in Table 3 and are obtained from common relations.^{64–69} The

Table 3. Calculated Elastic Constants C_{nm} , Bulk (B), Shear (G), and Young's (Y) Moduli (GPa), Debye Temperature (θ_D , K), and Poisson's Ratio (ν) for $\text{Li}_4\text{Sr}_4[\text{Si}_4\text{O}_4\text{N}_6]\text{O}^a$

| elastic moduli | | elastic constants | |
|----------------|-------|-------------------|-------|
| B_V | 114.8 | C_{11} | 230.4 |
| B_R | 107.4 | C_{22} | 230.4 |
| B_{VRH} | 111.1 | C_{33} | 174.4 |
| G_V | 70.0 | C_{44} | 47.8 |
| G_R | 62.0 | C_{55} | 47.8 |
| G_{VRH} | 65.9 | C_{66} | 108.8 |
| Y_{VRH} | 165.1 | C_{12} | 117.5 |
| ν | 0.25 | C_{13} | 40.6 |
| θ_D | 592.2 | C_{23} | 40.6 |

^aBulk and shear moduli according to the Voigt (B_V and G_V), Reuss (B_R and G_R), and Voigt–Reuss–Hill (B_{VRH} and G_{VRH}) approaches. The subscripts in C_{nm} were obtained from C_{ijkl} according to the Voigt notation $xx \rightarrow 1$, $yy \rightarrow 2$, $zz \rightarrow 3$, $yz \rightarrow 4$, $zx \rightarrow 5$, and $xy \rightarrow 6$.

calculations of elastic constants are in line with the layered structure of $\text{Li}_4\text{Sr}_4[\text{Si}_4\text{O}_4\text{N}_6]\text{O}$ because C_{11} and C_{22} (a and b directions) are significantly increased and less compressible with respect to C_{33} (c direction). The Debye temperature (θ_D) is a prominent proxy for phosphor materials, denoting the rigidity of the crystal.^{70–72} An increase in θ_D formally equates to an increase in rigidity and concomitantly energetically elevated lattice vibrations, which are harder to excite. Dopant atoms such as Eu^{2+} exhibiting transitions to protruding Eu 5d orbitals upon excitation should, therefore, be less likely affected by electron–phonon coupling effects with the host structure if embedded in a highly rigid network of anions. Compared to nitride compounds with higher condensation degrees such as $\text{SrLiAl}_3\text{N}_4$ ($\theta_D = 716$ K) or $\text{Sr}_2\text{Si}_5\text{N}_8$ ($\theta_D = 702$ K),⁷² the lower θ_D value of 592 K for $\text{Li}_4\text{Sr}_4[\text{Si}_4\text{O}_4\text{N}_6]\text{O}:\text{Eu}^{2+}$, while reflecting both the low bulk and shear moduli in line with the layered nature of $\text{Li}_4\text{Sr}_4[\text{Si}_4\text{O}_4\text{N}_6]\text{O}:\text{Eu}^{2+}$, can possibly indicate an attenuated thermal quenching.

UV/Vis Spectroscopy. The optical band gap was determined by UV/vis spectroscopy on a nondoped sample of $\text{Li}_4\text{Sr}_4[\text{Si}_4\text{O}_4\text{N}_6]\text{O}$. The diffuse-reflectance spectrum is shown in Figure 8 together with insets of a pseudoabsorption spectrum obtained by transformation via the Kubelka–Munk formalism.^{73–76} The diffuse-reflectance spectra show broad absorption ranging from 260 to 380 nm. The slight indent starting from 280 nm is attributed to natural defect states in the band gap possibly arising from the observed stacking faults. This is in line with the fact that dopant levels of about 1 mol % Eu in $\text{Li}_4\text{Sr}_4[\text{Si}_4\text{O}_4\text{N}_6]\text{O}$, resulting in distinct 4f and 5d states within the band gap, lead to a more pronounced effect in the same range of the spectrum (Figure S6). The optical band gap was subsequently derived by fitting the first ascent of the pseudoabsorption $[F(R)h\nu]^{1/n}$ and taking its inflection point with the energy scale. The resulting band gap of $\text{Li}_4\text{Sr}_4[\text{Si}_4\text{O}_4\text{N}_6]\text{O}$ is approximately 3.6 eV for indirect and 4.25 eV for direct transitions, agreeing well with band structure calculations favoring indirect transitions by about 0.6 eV (Figure S7). The value for direct transitions is in better correspondence with the obtained electronic band gap by DFT of approximately 4.4 eV. A higher value for the electronic band gap is to be expected because of the core–hole effect. Further, the stacking disorder in $\text{Li}_4\text{Sr}_4[\text{Si}_4\text{O}_4\text{N}_6]\text{O}$ might lower the band gap with regard to the fully ordered model from DFT

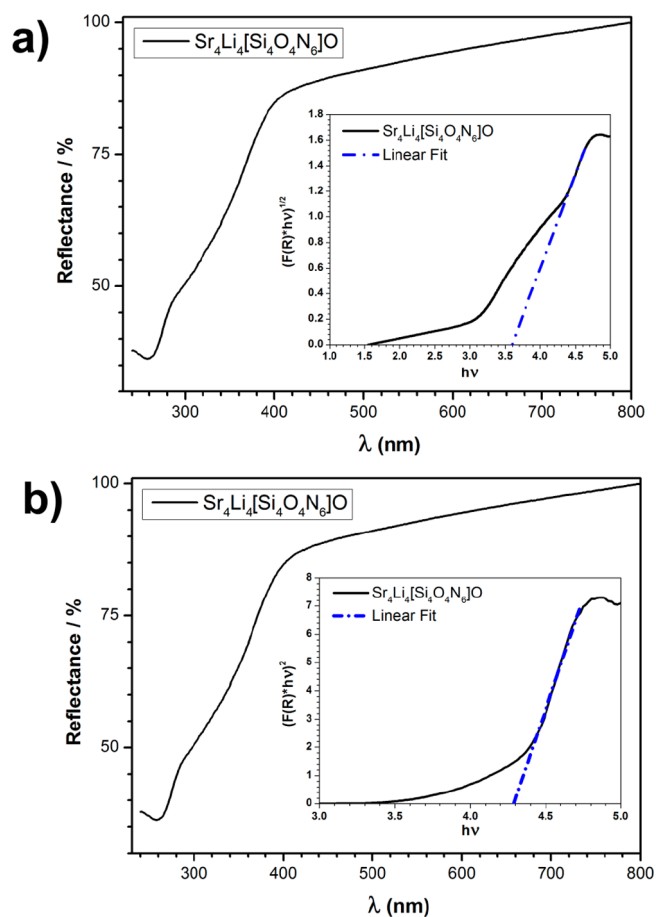


Figure 8. Diffuse-reflectance spectra of undoped $\text{Li}_4\text{Sr}_4[\text{Si}_4\text{O}_4\text{N}_6]\text{O}$ with insets of the respective Tauc plots $[F(R)h\nu]^{1/n}$ for (a) indirect ($n = 2$) and (b) direct ($n = 1/2$) band gaps. Linear fit in order to determine E_g in blue.

calculations because of the possible introduction of defect states.

Luminescence. Luminescence measurements were performed on thick-bed powder samples of Eu^{2+} -doped $\text{Li}_4\text{Sr}_4[\text{Si}_4\text{O}_4\text{N}_6]\text{O}$ in air. Excitation of the samples with UV-to-blue light leads to a broad-band emission in the orange spectral range. The excitation and emission spectra of a sample with a nominal doping content of 1 mol % referred to Sr are shown in Figure 9. The excitation spectrum exhibits a broad band with a maximum at around 410–425 nm, enabling the phosphor to be efficiently excited by blue-emitting (In,Ga)N-LEDs. The emission spectrum peaks at 625 nm and exhibits a full width at half-maximum (fwhm) of 4164 cm^{-1} (160 nm), surpassing that of $\text{YAG}:\text{Ce}^{3+}$ (fwhm $\approx 3700\text{ cm}^{-1}$; 120 nm).⁷⁷

A broad-band emission is observed for $\text{Li}_4\text{Sr}_4[\text{Si}_4\text{O}_4\text{N}_6]\text{O}:\text{Eu}^{2+}$, as seen from Figure 9, despite featuring only one crystallographic Sr/Eu site. A possible impact of side phases could be ruled out from single-crystal luminescence measurements showing identical emission behavior, as seen from Figure S8. A nearly Gaussian-shaped emission band on the energy scale is observed, which indicates a large Huang–Rhys parameter, corresponding to strong electron–phonon coupling.⁷⁸

Figure 10 shows the rather asymmetric coordination of Sr by O and N ions paired with the relatively unidimensional Sr displacement ellipsoid toward the noncoordinating O2 ($d_{\text{Sr-O}2}$

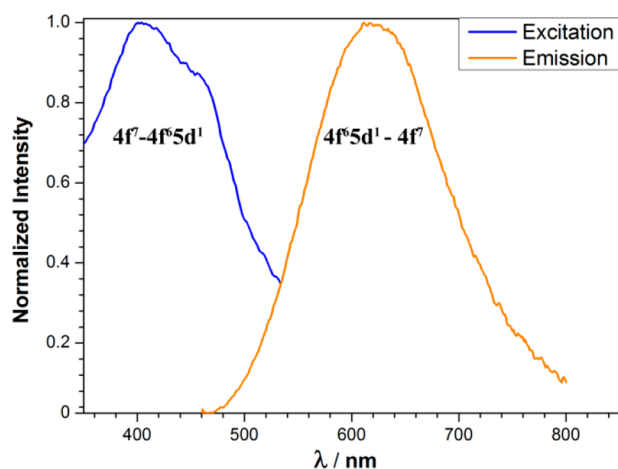


Figure 9. Excitation (blue) and emission (orange; $\lambda_{\text{exc}} = 440$ nm) spectra of bulk phase $\text{Li}_4\text{Sr}_4[\text{Si}_4\text{O}_4\text{N}_6]\text{O}:\text{Eu}^{2+}$ with a nominal dopant concentration of 1 mol %.

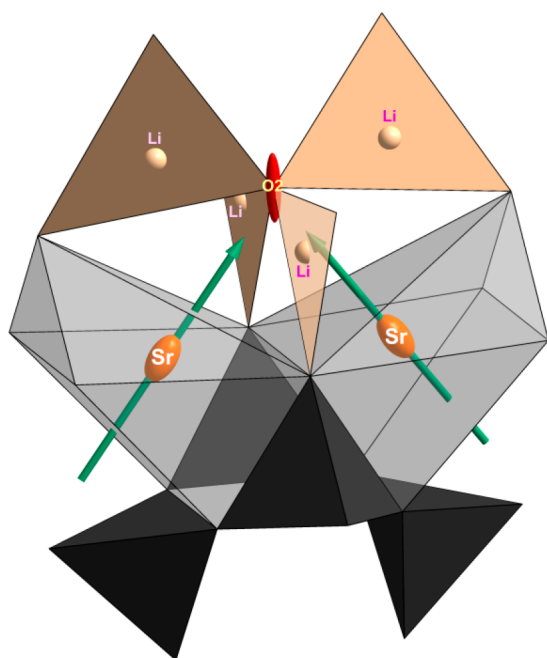


Figure 10. Coordination spheres of the Sr/Eu site (orange) in $\text{Li}_4\text{Sr}_4[\text{Si}_4\text{O}_4\text{N}_6]\text{O}$ with schematic displacement vectors (green arrows). Displacement ellipsoids are shown with 90% probability. Color code: SiN_3O tetrahedra, black; Sr/Eu coordination polyhedra, gray; Li, ivory; O, red.

= 3.11 Å) position. The observed stacking disorder, observed from PXRD and TEM investigations, is likely to impact the local environment even further. Because the crystal field of the spacious 5d orbitals, involved in the electronic $4f^7-4f^65d^1$ transitions in Eu^{2+} , is prone to strong local distortions, an explanation for the observed broadening of emission, further enhanced by strong electron–phonon coupling, can hence be inferred. The color coordinates according to the CIE 1931 convention are $x = 0.534$ and $y = 0.450$ and are depicted in Figure 11.

From Figure 11, it can be seen that the color point of $\text{Li}_4\text{Sr}_4[\text{Si}_4\text{O}_4\text{N}_6]\text{O}:\text{Eu}^{2+}$ lies in the orange spectral region close to the planckian locus. We estimated the correlated color

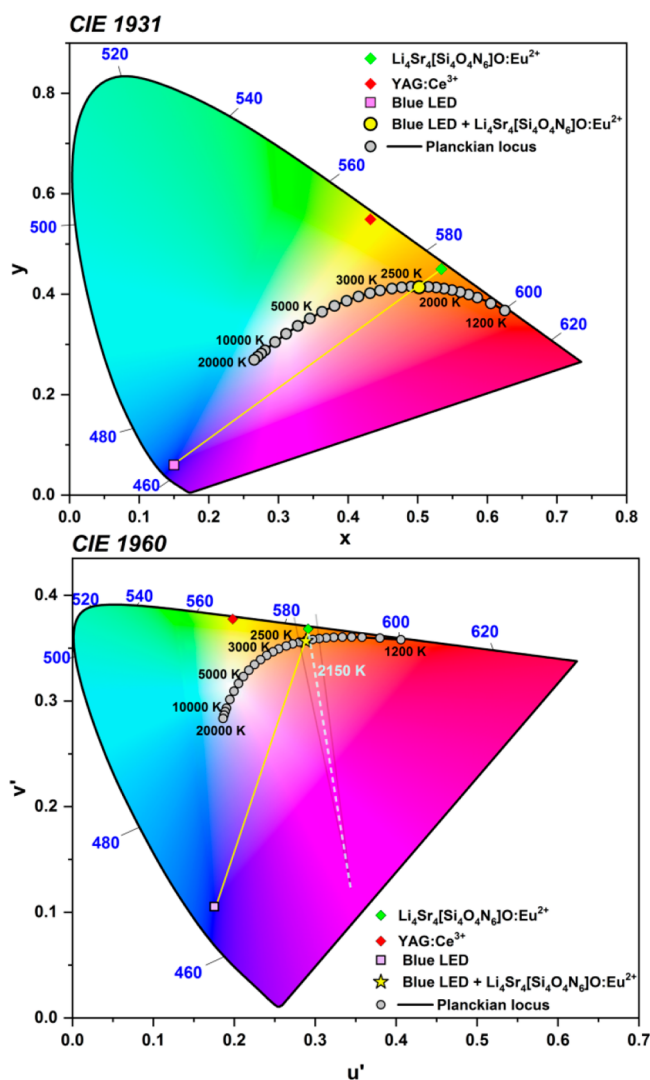


Figure 11. CIE 1931 (top) and CIE 1960 (bottom) color spaces showing the CIE coordinates of $\text{Li}_4\text{Sr}_4[\text{Si}_4\text{O}_4\text{N}_6]\text{O}:\text{Eu}^{2+}$ along with $\text{YAG}:\text{Ce}^{3+}$, a pure blue LED, and those of an ideal blackbody radiator at different temperatures (K). CCT of a single-phosphor LED indicated as ☆ on the yellow conjugation line alongside a construction to determine the CCT of the phosphor material itself (dotted gray intersection of the planckian locus in CIE 1960).⁷⁹

temperature (CCT) of the phosphor to be around 2150 K from the CIE 1960 diagram according to

$$\text{CCT} = \left[\frac{1}{T_i} + \frac{\theta_1}{\theta_2} \left(\frac{1}{T_{i+1}} - \frac{1}{T_i} \right) \right]^{-1}$$

where T_i and T_{i+1} correspond to the isothermals of the planckian CCT of the higher and lower isothermals and θ_1 to the angle between those isothermals. θ_2 corresponds to the angle between the higher CCT isothermal and the line drawn from the color point to the isothermal interception point.⁷⁹ The combination of a blue LED ($\lambda_{\text{em}} = 450$ nm) with $\text{Li}_4\text{Sr}_4[\text{Si}_4\text{O}_4\text{N}_6]\text{O}:\text{Eu}^{2+}$ would result in a CCT of ≈ 2200 K (candle light) and a CRI of 77.2 suitable for, e.g., decorative lighting applications.

Thermal Quenching. In order to determine the luminescence behavior of $\text{Li}_4\text{Sr}_4[\text{Si}_4\text{O}_4\text{N}_6]\text{O}:\text{Eu}^{2+}$, thermal quenching experiments were performed at low temperatures

(6–300 K) and up to typical LED operating temperatures (around 100–200 °C) by measuring the luminescence intensity and performing integration at each step. The thermal quenching behavior is shown in Figure 12, together with the

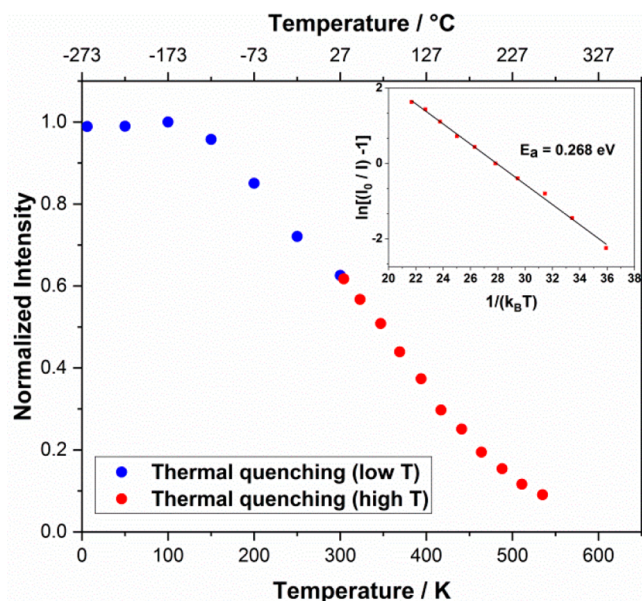


Figure 12. Thermal quenching measurements of $\text{Li}_4\text{Sr}_4[\text{Si}_4\text{O}_4\text{N}_6]\text{O}:\text{Eu}^{2+}$. The inset shows an Arrhenius plot of the thermal quenching data at elevated temperatures in order to determine the thermal activation energy E_a .

calculated thermal activation energy E_a obtained from an Arrhenius fit according to the equation

$$I = \frac{I_0}{1 + e^{E/kT}}$$

Here I_0 is the intensity at the beginning of measurement, k the Boltzmann constant (eV), T the temperature (K), and I the intensity at every following point of measurement.^{80,81} E_a is then obtained as the slope of the plot $\ln[(I_0/I) - 1]$ versus $1/kT$.

While the room temperature IQE was determined to be 24% (38% at 6 K), $\text{Li}_4\text{Sr}_4[\text{Si}_4\text{O}_4\text{N}_6]\text{O}:\text{Eu}^{2+}$ shows significant thermal quenching behavior at typical LED operating temperatures with $E_a = 0.268$ eV. This is subsequently significantly lower than that of commercial phosphors like $\text{YAG}:\text{Ce}^{3+}$ (0.81 eV).⁸² The observed behavior is in line with the strong electron–phonon coupling, which could correspond to the 4f–5d crossing model with increasing nonradiative emissions possibly paired with thermal ionization to the conduction band.⁸¹ The phosphor material is thus limited to a small application space of solid-state lighting, despite its attractive distribution of emission.

CONCLUSION

A suitable method for the discovery of novel materials is the screening of multicomponent mixtures. In this manner, the novel layered lithium oxonitridosilicate oxide $\text{Li}_4\text{Sr}_4[\text{Si}_4\text{O}_4\text{N}_6]\text{O}:\text{Eu}^{2+}$ has been obtained. Its structure formally derives from nonluminescent $\text{Li}_2\text{Sr}_4[\text{Si}_2\text{N}_5]\text{N}$ by means of O substitution and incorporation. The crystal structure was solved and refined from single-crystal X-ray data. Reproduction of the compound from optimized bulk syntheses was initially hindered by the

occurrence of broadened reflections with low intensity. TEM investigations prove to be a suitable tool in overcoming such challenges, revealing stacking disorder as a real structure phenomenon of the layered compound while corroborating the cell metrics. As a result, the broadening of some reflections observed in the PXRD patterns was successfully modeled through the introduction of stacking faults. $\text{Li}_4\text{Sr}_4[\text{Si}_4\text{O}_4\text{N}_6]\text{O}:\text{Eu}^{2+}$ contributes to the sparsely investigated class of lithium oxonitridosilicate(oxides), exemplifying paths to the discovery of novel phosphor materials, highlighting the importance of continuous research for compounds in this materials class. $\text{Li}_4\text{Sr}_4[\text{Si}_4\text{O}_4\text{N}_6]\text{O}:\text{Eu}^{2+}$ shows emission in the yellow-to-orange spectral range featuring an indirect optical band gap of 3.6 eV. DFT calculations suggest an electronic band gap of about 4.4 eV for a model free from stacking faults. Calculations of the Debye temperature (592 K) reveal the highest mechanical compressibility along the [001] direction, in line with the layered structure of $\text{Li}_4\text{Sr}_4[\text{Si}_4\text{O}_4\text{N}_6]\text{O}$. The emission of $\text{Li}_4\text{Sr}_4[\text{Si}_4\text{O}_4\text{N}_6]\text{O}:\text{Eu}^{2+}$ is likely broadened because of large electron–phonon coupling and concomitant stacking faults between layers, as seen from the broadened Gaussian-shaped emission profile. This, in turn, corroborates the use of θ_D as a preliminary proxy when estimating the efficiency of a possible phosphor host material beforehand. The synthesis and subsidiary analytical approaches like TEM investigations of $\text{Li}_4\text{Sr}_4[\text{Si}_4\text{O}_4\text{N}_6]\text{O}:\text{Eu}^{2+}$ further exemplify how optimization, characterization, and in-depth illumination of real-structure phenomena can interlock and help to push the understanding of materials property relationships and phosphor materials research approaches in general.

ASSOCIATED CONTENT

Supporting Information

The Supporting Information is available free of charge on the ACS Publications website at DOI: 10.1021/acs.inorgchem.8b02391.

IR, further TEM and EDX results, atomic coordinates, anisotropic displacement parameters, CHARDI results, modeled stacking faults, band structure, and single-crystal luminescence (PDF)

Accession Codes

CCDC 1862968 contains the supplementary crystallographic data for this paper. These data can be obtained free of charge via www.ccdc.cam.ac.uk/data_request/cif, or by emailing data_request@ccdc.cam.ac.uk, or by contacting The Cambridge Crystallographic Data Centre, 12 Union Road, Cambridge CB2 1EZ, UK; fax: +44 1223 336033.

AUTHOR INFORMATION

Corresponding Author

*E-mail: wolfgang.schnick@uni-muenchen.de (W.S.).

ORCID

Wolfgang Schnick: 0000-0003-4571-8035

Author Contributions

All authors have given approval to the final version of the manuscript.

Notes

The authors declare no competing financial interest.

ACKNOWLEDGMENTS

We thank Dr. Peter Mayer for collecting single-crystal data (LMU). Dr. Constantin Hoch is thanked for valuable discussions regarding single-crystal analysis along with Christian Maak and Philipp Bielec (all at LMU) for constructive discussions. Detlef Wiechert and Volker Weiler (both at Lumileds Phosphor Center Aachen) are thanked for performing temperature-dependent luminescence measurements and data processing. Prof. Dr. Oliver Oeckler (Institute for Mineralogy, Crystallography and Materials Science, Leipzig University) is thanked for contributory annotations. Financial support by the Fonds der Chemischen Industrie is gratefully acknowledged.

REFERENCES

- (1) Maak, C.; Strobel, P.; Weiler, V.; Schmidt, P. J.; Schnick, W. Unprecedented Deep-Red Ce^{3+} Luminescence of the Nitridolithosilicates $Li_{3.87}RE_{3.3}Ca_{5.7}[Li_2Si_3O_7N_{5.9}]O_2F$ ($RE = La, Ce, Y$). *Chem. Mater.* **2018**, *30*, 5500–5506.
- (2) Hirosaki, N.; Takeda, T.; Funahashi, S.; Xie, R.-J. Discovery of New Nitridosilicate Phosphors for Solid State Lighting by the Single-Particle-Diagnosis Approach. *Chem. Mater.* **2014**, *26*, 4280–4288.
- (3) Neudert, L.; Durach, D.; Fahrnbauer, F.; Vaughan, G. B. M.; Schnick, W.; Oeckler, O. Highly Symmetric AB₂ Framework Related to Tridymite in the Disordered Nitridosilicate $La_{2.4}Sr_{14-7x}[Si_{36}N_{72}]_{-}(O_{1-x}F_x)_{14}$ ($x = 0.489$). *Inorg. Chem.* **2017**, *56*, 13070–13077.
- (4) Strobel, P.; Weiler, V.; Hecht, C.; Schmidt, P. J.; Schnick, W. Luminescence of the Narrow-Band Red Emitting Nitridomagnesiumsilicate $Li_2(Ca_{1-x}Sr_x)_2[Mg_2Si_2N_6]:Eu^{2+}$ ($x = 0-0.06$). *Chem. Mater.* **2017**, *29*, 1377–1383.
- (5) Poesl, C.; Schnick, W. Crystal Structure and Nontypical Deep-Red Luminescence of $Ca_3Mg[Li_2Si_2N_6]:Eu^{2+}$. *Chem. Mater.* **2017**, *29*, 3778–3784.
- (6) Schmiechen, S.; Nietschke, F.; Schnick, W. Structural Relationship between the Mg-Containing Nitridosilicates $Ca_2Mg[Li_4Si_2N_6]$ and $Li_2Ca_2[Mg_2Si_2N_6]$. *Eur. J. Inorg. Chem.* **2015**, *2015*, 1592–1597.
- (7) Li, Y.; Wang, C.-A.; Xie, H.; Cheng, J.; Goodenough, J. B. High lithium ion conduction in garnet-type $Li_6La_3ZrTaO_{12}$. *Electrochem. Commun.* **2011**, *13*, 1289–1292.
- (8) Murugan, R.; Thangadurai, V.; Weppner, W. Fast Lithium Ion Conduction in Garnet-Type $Li_7La_3Zr_2O_{12}$. *Angew. Chem., Int. Ed.* **2007**, *46*, 7778–7781.
- (9) Wu, J.-F.; Pang, W. K.; Peterson, V. K.; Wei, L.; Guo, X. Garnet-Type Fast Li-Ion Conductors with High Ionic Conductivities for All-Solid-State Batteries. *ACS Appl. Mater. Interfaces* **2017**, *9*, 12461–12468.
- (10) Pagano, S.; Lupart, S.; Schmiechen, S.; Schnick, W. $Li_4Ca_3Si_2N_6$ and $Li_4Sr_3Si_2N_6$ – Quaternary Lithium Nitridosilicates with Isolated $[Si_2N_6]^{10-}$ Ions. *Z. Anorg. Allg. Chem.* **2010**, *636*, 1907–1909.
- (11) Wagatha, P.; Pust, P.; Weiler, V.; Wochnik, A. S.; Schmidt, P. J.; Scheu, C.; Schnick, W. $Ca_{18.75}Li_{10.5}[Al_{39}N_{55}]:Eu^{2+}$ —Supertetrahedron Phosphor for Solid-State Lighting. *Chem. Mater.* **2016**, *28*, 1220–1226.
- (12) Pust, P.; Weiler, V.; Hecht, C.; Tücks, A.; Wochnik, A. S.; Henß, A.-K.; Wiechert, D.; Scheu, C.; Schmidt, P. J.; Schnick, W. Narrow-band red-emitting $Sr[LiAl_3N_4]:Eu^{2+}$ as a next-generation LED-phosphor material. *Nat. Mater.* **2014**, *13*, 891–896.
- (13) Wilhelm, D.; Baumann, D.; Seibald, M.; Wurst, K.; Heymann, G.; Huppertz, H. Narrow-Band Red Emission in the Nitridolithoaluminate $Sr_4[LiAl_{11}N_{14}]:Eu^{2+}$. *Chem. Mater.* **2017**, *29*, 1204–1209.
- (14) Li, Y. Q.; Hirosaki, N.; Xie, R. J.; Takeka, T.; Mitomo, M. Crystal, electronic structures and photoluminescence properties of rare-earth doped $LiSi_2N_3$. *J. Solid State Chem.* **2009**, *182*, 301–311.
- (15) Strobel, P.; Schmiechen, S.; Siegert, M.; Tücks, A.; Schmidt, P. J.; Schnick, W. Narrow-Band Green Emitting Nitridolithoalumosilicate $Ba[Li_2(Al_2Si_2)N_6]:Eu^{2+}$ with Framework Topology whj for LED/LCD-Backlighting Applications. *Chem. Mater.* **2015**, *27*, 6109–6115.
- (16) Takeda, T.; Hirosaki, N.; Funahashi, S.; Xie, R.-J. Narrow-Band Green-Emitting Phosphor $Ba_2LiSi_7AlN_{12}:Eu^{2+}$ with High Thermal Stability Discovered by a Single Particle Diagnosis Approach. *Chem. Mater.* **2015**, *27*, 5892–5898.
- (17) Xie, R.-J.; Hirosaki, N.; Li, H.-L.; Li, Y. Q.; Mitomo, M. Synthesis and Photoluminescence Properties of β -sialon: Eu^{2+} ($Si_{6-z}Al_zOzN_{8-z}:Eu^{2+}$): A Promising Green Oxynitride Phosphor for White Light-Emitting Diodes. *J. Electrochem. Soc.* **2007**, *154*, J314–J319.
- (18) Hirosaki, N.; Xie, R.-J.; Kimoto, K.; Sekiguchi, T.; Yamamoto, Y.; Suehiro, T.; Mitomo, M. Characterization and properties of green-emitting β -SiAlON: Eu^{2+} powder phosphors for white light-emitting diodes. *Appl. Phys. Lett.* **2005**, *86*, 211905.
- (19) Li, S.; Wang, L.; Tang, D.; Cho, Y.; Liu, X.; Zhou, X.; Lu, L.; Zhang, L.; Takeda, T.; Hirosaki, N.; Xie, R.-J. Achieving High Quantum Efficiency Narrow-Band β -Sialon: Eu^{2+} Phosphors for High-Brightness LCD Backlights by Reducing the Eu^{3+} Luminescence Killer. *Chem. Mater.* **2018**, *30*, 494–505.
- (20) Seibald, M.; Oeckler, O.; Celinski, V. R.; Schmidt, P. J.; Tücks, A.; Schnick, W. Real structure and diffuse scattering of $Sr_{0.5}Ba_{0.5}Si_2O_2N_2:Eu^{2+}$ - A highly efficient yellow phosphor for pc-LEDs. *Solid State Sci.* **2011**, *13*, 1769–1778.
- (21) Seibald, M.; Rosenthal, T.; Oeckler, O.; Maak, C.; Tücks, A.; Schmidt, P. J.; Wiechert, D.; Schnick, W. New Polymorph of the Highly Efficient LED-Phosphor $SrSi_2O_2N_2:Eu^{2+}$ – Polyttypism of a Layered Oxonitridosilicate. *Chem. Mater.* **2013**, *25*, 1852–1857.
- (22) Maak, C.; Hoch, C.; Schmidt, P. J.; Schnick, W. Oxonitridosilicate Oxides $RE_2Ba_6[Si_{22}O_{19}N_{36}]O_{16}:Eu^{2+}$ ($RE = Y, Tb$) with a Unique Layered Structure and Orange-Red Luminescence for $RE = Y$. *Inorg. Chem.* **2018**, *57*, 2242–2248.
- (23) Seibald, M.; Rosenthal, T.; Oeckler, O.; Schnick, W. Highly Efficient pc-LED Phosphors $Sr_{1-x}Ba_xSi_2O_2N_2:Eu^{2+}$ ($0 < x < 1$) - Crystal Structures and Luminescence Properties Revisited. *Crit. Rev. Solid State Mater. Sci.* **2014**, *39*, 215–229.
- (24) Kloß, S. D.; Neudert, L.; Döblinger, M.; Nentwig, M.; Oeckler, O.; Schnick, W. Puzzling Intergrowth in Cerium Nitridophosphate Unraveled by Joint Venture of Aberration-Corrected Scanning Transmission Electron Microscopy and Synchrotron Diffraction. *J. Am. Chem. Soc.* **2017**, *139*, 12724–12735.
- (25) Lange, H.; Wötting, G.; Winter, G. Silicon Nitride—From Powder Synthesis to Ceramic Materials. *Angew. Chem., Int. Ed. Engl.* **1991**, *30*, 1579–1597.
- (26) Hofman-Bang, N.; et al. Preparation of Lithium Azide. *Acta Chem. Scand.* **1957**, *11*, 581–582.
- (27) Sheldrick, G. M. SADABS, version 2: Multi-Scan Absorption Correction; Bruker-AXS: Billerica, MA, 2012.
- (28) Sheldrick, G. M. SHELXS-97: A Program for Crystal Structure Solution; University of Göttingen: Göttingen, Germany, 1997.
- (29) Sheldrick, G. M. SHELXL-97: A Program for Crystal Structure Refinement; University of Göttingen: Göttingen, Germany, 1997.
- (30) Sheldrick, G. M. A short history of SHELX. *Acta Crystallogr., Sect. A: Found. Crystallogr.* **2008**, *64*, 112–122.
- (31) Rietveld, H. A profile refinement method for nuclear and magnetic structures. *J. Appl. Crystallogr.* **1969**, *2*, 65–71.
- (32) Coelho, A. A. TOPAS 4.1: A program for Rietveld refinement; Coelho Software: Brisbane, Australia, 2007.
- (33) Bergmann, J.; Kleeberg, R.; Haase, A.; Breidenstein, B. Advanced Fundamental Parameters Model for Improved Profile Analysis. *Mater. Sci. Forum* **2000**, *347–349*, 303–308.
- (34) Cheary, R. W.; Coelho, A. A.; Cline, J. P. Fundamental Parameters Line Profile Fitting in Laboratory Diffractometers. *J. Res. Natl. Inst. Stand. Technol.* **2004**, *109*, 1–25.
- (35) Le Bail, A.; Jouxneaux, A. A Qualitative Account for Anisotropic Broadening in Whole-Powder-Diffraction-Pattern Fitting by Second-Rank Tensors. *J. Appl. Crystallogr.* **1997**, *30*, 265–271.
- (36) Kresse, G.; Hafner, J. *Ab initio* molecular dynamics for liquid metals. *Phys. Rev. B: Condens. Matter Mater. Phys.* **1993**, *47*, 558.

- (37) Kresse, G.; Hafner, J. *Ab initio* molecular-dynamics simulation of the liquid-metal-amorphous-semiconductor transition in germanium. *Phys. Rev. B: Condens. Matter Mater. Phys.* **1994**, *49*, 14251.
- (38) Kresse, G.; Furthmüller, J. Efficiency of *ab-initio* total energy calculations for metals and semiconductors using a plane-wave basis set. *Comput. Mater. Sci.* **1996**, *6*, 15–50.
- (39) Perdew, J. P.; Burke, K.; Ernzerhof, M. Generalized Gradient Approximation Made Simple. *Phys. Rev. Lett.* **1996**, *77*, 3865.
- (40) Perdew, J. P.; Burke, K.; Ernzerhof, M. Generalized Gradient Approximation Made Simple. *Phys. Rev. Lett.* **1996**, *77*, 3865.
- (41) Blöchl, P. E. Projector augmented-wave method. *Phys. Rev. B: Condens. Matter Mater. Phys.* **1994**, *50*, 17953.
- (42) Kresse, G.; Joubert, D. From ultrasoft pseudopotentials to the projector augmented-wave method. *Phys. Rev. B: Condens. Matter Mater. Phys.* **1999**, *59*, 1758.
- (43) Monkhorst, H. J.; Pack, J. D. Special points for Brillouin-zone integrations. *Phys. Rev. B* **1976**, *13*, 5188.
- (44) Becke, A. D.; Johnson, E. R. A simple effective potential for exchange. *J. Chem. Phys.* **2006**, *124*, 221101.
- (45) Tran, F.; Blaha, P. Accurate Band Gaps of Semiconductors and Insulators with a Semilocal Exchange-Correlation Potential. *Phys. Rev. Lett.* **2009**, *102*, 226401.
- (46) Camargo-Martínez, J. A.; Baquero, R. Performance of the modified Becke-Johnson potential for semiconductors. *Phys. Rev. B: Condens. Matter Mater. Phys.* **2012**, *86*, 195106.
- (47) Le Page, Y.; Saxe, P. Symmetry-general least-squares extraction of elastic data for strained materials from *ab initio* calculations of stress. *Phys. Rev. B: Condens. Matter Mater. Phys.* **2002**, *65*, 104104.
- (48) *Digital Micrograph*, version 3.6.1; Gatan: Warrendale, PA, 1999.
- (49) Lábár, J. L. Consistent indexing of a (set of) single crystal SAED pattern(s) with the ProcessDiffraction program. *Ultramicroscopy* **2005**, *103*, 237–249.
- (50) Stadelmann, P. A. *JEMS*, version 3.3425; CIME–EPFL: Ecublens, Switzerland, 2008.
- (51) *ES Vision*, version 4.0.164; Emispec Systems Inc.: Tempe, AZ, 2002.
- (52) Irran, E.; Köllisch, K.; Leoni, S.; Nesper, R.; Henry, P. F.; Weller, M. T.; Schnick, W. $\text{Ce}_4[\text{Si}_4\text{O}_4\text{N}_6]\text{O}$ -A Hyperbolically Layered Oxonitridosilicate Oxide with an Ordered Distribution of Oxygen and Nitrogen. *Chem. - Eur. J.* **2000**, *6*, 2714–2720.
- (53) Lupart, S.; Pagano, S.; Oeckler, O.; Schnick, W. $\text{Li}_2\text{Sr}_4[\text{Si}_2\text{N}_5]\text{N}$ – A Layered Lithium Nitridosilicate Nitride. *Eur. J. Inorg. Chem.* **2011**, *2011*, 2118–2123.
- (54) Oeckler, O.; Stadler, F.; Rosenthal, T.; Schnick, W. Real structure of $\text{SrSi}_2\text{O}_7\text{N}_2$. *Solid State Sci.* **2007**, *9*, 205–212.
- (55) Pagano, S.; Lupart, S.; Zeuner, M.; Schnick, W. Tuning the Dimensionality of Nitridosilicates in Lithium Melts. *Angew. Chem.* **2009**, *121*, 6453–6456.
- (56) Treacy, M. M. J.; Newsam, J. M.; Deem, M. W. A general recursion method for calculating diffracted intensities from crystals containing planar faults. *Proc. R. Soc. London, Ser. A* **1991**, *433*, 499–520.
- (57) Shannon, R. Revised effective ionic radii and systematic studies of interatomic distances in halides and chalcogenides. *Acta Crystallogr., Sect. A: Cryst. Phys., Diffraction, Theor. Gen. Crystallogr.* **1976**, *32*, 751–767.
- (58) Hoppe, R. Madelung Constants. *Angew. Chem., Int. Ed. Engl.* **1966**, *5*, 95–106.
- (59) Hoppe, R. The Coordination Number – an “Inorganic Chameleon”. *Angew. Chem., Int. Ed. Engl.* **1970**, *9*, 25–34.
- (60) Hübenthal, R. *MAPLE, Program for the Calculation of MAPLE values*, version 4; University of Gießen: Gießen, Germany, 1993.
- (61) Zeuner, M. P. S.; Pagano, S.; Schnick, W. Nitridosilicates and Oxonitridosilicates: From Ceramic Materials to Structural and Functional Diversity. *Angew. Chem., Int. Ed.* **2011**, *50*, 7754–7775.
- (62) Kechele, J. A.; Schmolke, C.; Lupart, S.; Schnick, W. $\text{Ln}_3[\text{SiON}_3]\text{O}$ (Ln = La, Ce, Pr) – Three Oxonitridosilicate Oxides with Crystal Structures Derived from the Anti-Perovskite Structure Type. *Z. Anorg. Allg. Chem.* **2010**, *636*, 176–182.
- (63) Maak, C.; Niklaus, R.; Friedrich, F.; Mähringer, A.; Schmidt, P. J.; Schnick, W. Efficient Yellow-Orange Phosphor $\text{Lu}_4\text{Ba}_2[\text{Si}_9\text{ON}_{16}]\text{O}:\text{Eu}^{2+}$ and Orange-Red Emitting $\text{Y}_4\text{Ba}_2[\text{Si}_9\text{ON}_{16}]\text{O}:\text{Eu}^{2+}$: Two Oxonitridosilicate Oxides with Outstanding Structural Variety. *Chem. Mater.* **2017**, *29*, 8377–8384.
- (64) Ashcroft, N. W.; Mermin, N. D. *Solid state physics*; Saunders College: Philadelphia, PA, 1976.
- (65) Hill, R. The Elastic Behaviour of a Crystalline Aggregate. *Proc. Phys. Soc., London, Sect. A* **1952**, *65*, 349–354.
- (66) Jiang, C.; Srinivasan, S. G.; Caro, A.; Maloy, S. A. Structural, elastic, and electronic properties of Fe_3C from first principles. *J. Appl. Phys.* **2008**, *103*, 043502.
- (67) Francisco, E.; Recio, J. M.; Blanco, M. A.; Pendás, A. M.; Costales, A. Quantum-Mechanical Study of Thermodynamic and Bonding Properties of MgF_2 . *J. Phys. Chem. A* **1998**, *102*, 1595–1601.
- (68) Francisco, E.; Blanco, M. A.; Sanjurjo, G. Atomistic simulation of SrF_2 polymorphs. *Phys. Rev. B: Condens. Matter Mater. Phys.* **2001**, *63*, 094107.
- (69) Poirier, J.-P. *Introduction to the physics of the earth's interior*; Cambridge University Press: Cambridge, U.K., 1921.
- (70) Brgoch, J.; DenBaars, S. P.; Seshadri, R. Proxies from *Ab Initio* Calculations for Screening Efficient Ce^{3+} Phosphor Hosts. *J. Phys. Chem. C* **2013**, *117*, 17955–17959.
- (71) Denault, K. A.; Brgoch, J.; Kloß, S. D.; Gaultois, M. W.; Siewenie, J.; Page, K.; Seshadri, R. Average and Local Structure, Debye Temperature, and Structural Rigidity in Some Oxide Compounds Related to Phosphor Hosts. *ACS Appl. Mater. Interfaces* **2015**, *7*, 7264–7272.
- (72) Wang, Z.; Chu, I.-H.; Zhou, F.; Ong, S. P. Electronic Structure Descriptor for the Discovery of Narrow-Band Red-Emitting Phosphors. *Chem. Mater.* **2016**, *28*, 4024–4031.
- (73) Kubelka, P.; Munk, F. Ein Beitrag Zur Optik Der Farbenstriche. *Z. Technol. Phys.* **1931**, *12*, 593–601.
- (74) Kubelka, P. New Contributions to the Optics of Intensely Light-Scattering Materials. Part I. *J. Opt. Soc. Am.* **1948**, *38*, 448–457.
- (75) Tauc, J.; Grigorovici, R.; Vancu, A. Optical Properties and Electronic Structure of Amorphous Germanium. *Phys. Status Solidi B* **1966**, *15*, 627–637.
- (76) López, R.; Gómez, R. Band-gap energy estimation from diffuse reflectance measurements on sol–gel and commercial TiO_2 : a comparative study. *J. Sol-Gel Sci. Technol.* **2012**, *61*, 1–7.
- (77) Moriguchi, T.; Noguchi, Y.; Sakanao, K.; Shimizu, Y. U.S. Patent 5,998,925A, 1997.
- (78) Henderson, B.; Imbusch, G. *Optical Spectroscopy of Inorganic Solids*; Clarendon Press, 1989.
- (79) *Optical Testing for SuperFlux, SnapLED and LUXEON®Emitters*; Philips Lumileds: Application Brief AB08, 2006.
- (80) Pavitra, E.; Su Yu, J. Luminescent properties of Gd^{3+} sensitized low-phonon energy $\text{CaGd}_2\text{O}_7:\text{Tb}^{3+}$ green emitting novel phosphors. *Ceram. Int.* **2013**, *39*, 1029–1036.
- (81) Qin, X.; Liu, X.; Huang, W.; Bettinelli, M.; Liu, X. Lanthanide-Activated Phosphors Based on 4f-5d Optical Transitions: Theoretical and Experimental Aspects. *Chem. Rev.* **2017**, *117*, 4488–4527.
- (82) Ueda, J.; Dorenbos, P.; Bos, A. J. J.; Kuroishi, K.; Tanabe, S. Control of electron transfer between Ce^{3+} and Cr^{3+} in the $\text{Y}_3\text{Al}_{5-x}\text{Ga}_x\text{O}_{12}$ host via conduction band engineering. *J. Mater. Chem. C* **2015**, *3*, 5642–5651.